Toward 4C FWI: DAS and 3C as complementary datasets

Matt Eaid and Kris Innanen

ABSTRACT

Full waveform inversion (FWI) is a useful, and powerful tool for finding accurate estimates of subsurface properties. However, when applied to conventional land data, the quality of the inversion can suffer from nonideal acquisition. FWI is most successful when we have densely sampled, wide aperture data, with a large bandwidth. Seismic data acquired with standard three component (3C) geophones typically lacks the low frequencies and dense sampling required for successful inversions. Recent advances, in the use of distributed acoustic sensors (DAS), may hold the key to remediation of these problems. Distributed acoustic sensors employ a continuous optical fibre, offering tighter spatial sampling at a greatly reduced cost, especially in the borehole environment. It has also been shown in laboratory experiments, that DAS fibres can recover significantly lower frequencies than standard 3C geophones. The trade-off, however, is that DAS fibres only sense strain along their tangent and therefore only provide one wavefield component, at a lower signal-to-noise ratio, limiting our ability to invert for elastic parameters. Taken together, both datasets share complementary aspects that should benefit FWI.

In September of 2018, CREWES in partnership with the Containment and Monitoring Institute (CaMI), acquired a large 3D walkaway-walkaround VSP dataset into both straight fibre, helical fibre, and 3C geophones in our geophysics well. Future work will focus on utilization of this dataset to develop an FWI formulation that leverages the complementary aspects of the DAS and geophone data. This paper is concerned with exploring the modelling of these complementary aspects as they relate to FWI, using the CaMI field site as our model.

INTRODUCTION

Full waveform inversion attempts to find high resolution models of subsurface properties by updating the model, such that the predicted data is driven towards the observed data (Lailly, 1983; Tarantola, 1984; Pratt et al., 1998; Virieux and Operto, 2009). Classic formulations of FWI have found success by minimizing an objective function that is dependent on the L_2 norm of the data residuals. Despite these successes, and the fact that FWI is becoming increasingly popular within the industry, formulations of this kind face significant challenges.

One of the main challenges for classic FWI is known as cycle skipping, and results from predicted data that are phase shifted from the observed data by more than a half cycle. Cycle skipping arises when our postulated model is a poor representation of the true subsurface and generally leads to a locally optimized objective function that produces a less accurate model than the starting model. The multiscale approach (Bunks, 1995) remedies this problem by starting the inversion from low frequencies, and then widens the bandwidth once the long wavelength model has been recovered. However, in order to implement this approach the data must contain sufficiently low frequencies, such that, at the lowest frequency the observed and predicted data match to within a half cycle.

Because geophones operate based on a mass attached to a spring, they are akin to simple harmonic oscillators having a resonant frequency dependent on the inverse square root of the mass. Below the resonant frequency geophones struggle to record meaningful signal. This frequency can be pushed lower by increasing the mass, however this has generally shown to be impractical. Because geophones struggle to capture these low frequencies, many current and legacy datasets lack the low frequencies necessary for full waveform inversion to be successful. In these cases, the multiscale approach will not be effective in helping FWI overcome cycle skipping.

Spatial sampling presents an additional challenge in recovering high resolution models of subsurface parameters. It is expensive and challenging to deploy geophones in dense arrays, especially in boreholes. The result is that most exploration level seismic surveys lack the dense spatial sampling required for certain applications of full waveform inversion. Studies have shown that the successful imaging of surface waves, a necessity for near surface velocity inversion, requires very dense sampling that is not seen in exploration programs (Park et al., 2002). Data interpolation can improve inversions, however, dense sampling still provides superior results (Mills, 2017).

A relatively new, and growing technology, known as distributed acoustic sensing (DAS) has the potential to remedy the challenges associated with conventional seismic data, as it relates to FWI. Employing a standard, cost-effective, telecommunication optical fibre allows distributed acoustic sensors to be deployed continuously over the entire length of the well providing significantly denser sampling. Laboratory and field studies have also shown the ability of distributed acoustic sensors to record seismic data with a lower frequency floor than geophones (Jin and Roy, 2017; Becker et al., 2018). The ability of DAS to supply lower frequency data at a denser sampling makes it a prime candidate to help aid full waveform inversion algorithms in their search for high resolution subsurface models.

Despite these improvements distributed acoustic sensing data on its own is not expected to recover accurate models of elastic parameters. In order to recover elastic parameters, particularly shear wave velocity, we need to record, and model, three component seismic data. The fibres in distributed acoustic sensors only record strain along their axial tangent, and therefore only supply one tangential component of the strain field. DAS also supplies seismic data at a generally lower signal-to-noise ratio than geophones, a detriment for full waveform inversion.

From a full waveform inversion perspective, distributed acoustic sensors and geophones share complementary aspects, that when coupled could make FWI more robust. How exactly to combine the datasets and formulate the objective function will be the focus of future work. In this paper we present complementary aspects in more detail and discuss how the two datasets could work together to improve the quality of our inversions.

In September of this year CREWES in partnership with CaMI acquired a 3D walkaway, walkaround VSP dataset to test this theory, amongst others. The source-receiver geometry from this survey is used to model both 3C and DAS data and compare them to the actual field data. The modeled data is then used to compare and contrast geophone and fibre data, and emphasize how they may complement each other within a FWI framework.

CONTAINMENT AND MONITORING INSTITUTE FIELD RESEARCH STATION

Carbon Management Canada (CMC) hosts two research institutes focused on carbon management within Canada's fossil fuels sector. The Containment and Monitoring Institute (CaMI) possesses a field research station (FRS) located approximately 150 km southeast of Calgary in Newell County, Alberta (figure 1). The main goal of this field research station is to study technologies for sequestration and monitoring of in situ carbon dioxide (CO_2). The site also serves the secondary goal of a sandbox for the creation of made-to-order datasets for design and appraisal of new geophysical acquisition, processing, and inversion technologies.

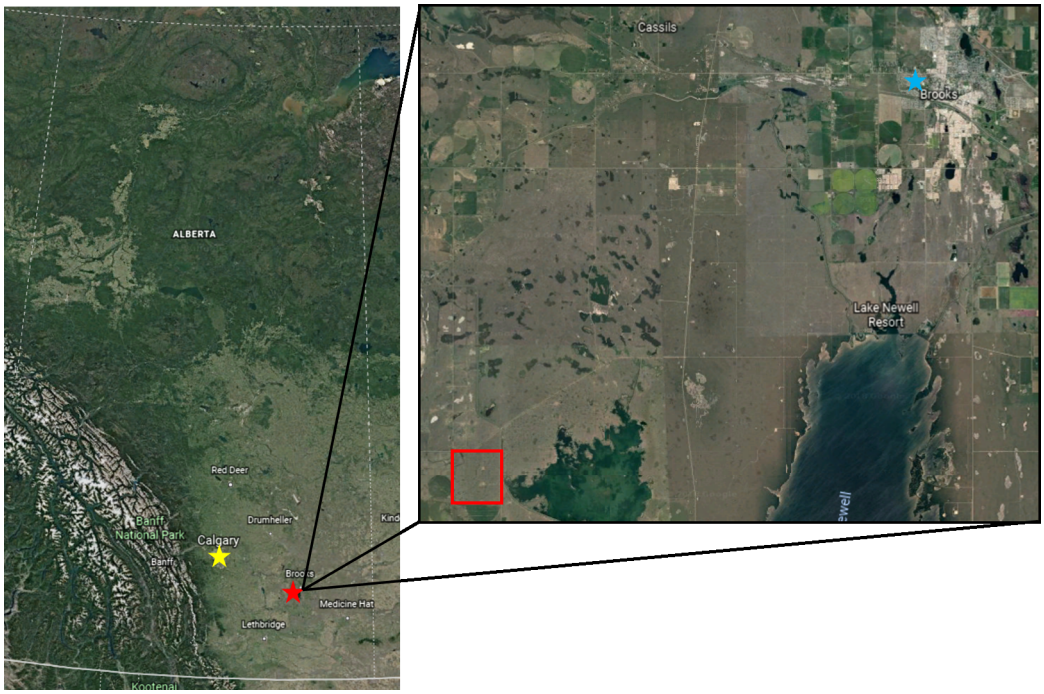

FIG. 1. Location of CaMI Field Research Station. (left) Location of the field research station (red star) in relation to Calgary, Alberta (yellow star). (right) Location of the field research station (red box) in relation to Brooks, Alberta (cyan star). Courtesy of Google Earth

Permanent installations at CaMI include an injector well, two observation wells outfitted with DAS fibre and permanent 3C geophones, a trench conatining buried DAS fibre, and a permanent buried array of 3C geophones Lawton et al. (2016). Of particular interest to this discussion is the fibre loop, which is one of only a few in the world to include both surface and borehole components, with both straight and helical fibre. Figure 2 shows a schematic diagram of the fibre loop installed at CaMI. The fibre runs from the interrogator to observation well 2 (geophysics well), and makes two loops over the length of the well, one with straight fibre and one with helical. It then runs from observation well 2 to observation well 1 (geochemistry well), and makes one loop using straight fibre. From observation well 1 the fibre runs to the trench, where a straight section, buried one meter deep, runs northeast to the end of the trench. The fibre reverses direction, and a helical section runs southwest along the entire 1.1 km length of the trench. A trenched section of straight fibre then runs back to the junction box at observation well 2, and then to the interrogator.

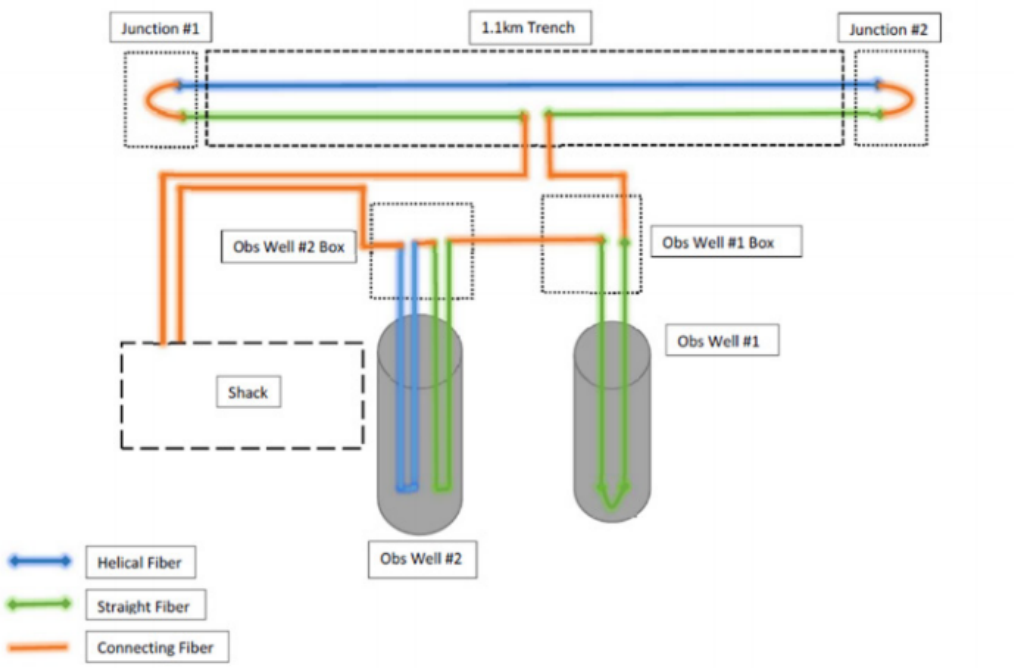

FIG. 2. Schematic diagram of fibre loop installed at the CaMI field research station in Newell County, Alberta (Lawton et al., 2016).

2018 3D VSP

In September of 2018 CREWES acquired an exploration scale walkaway-walkaround 3D vertical seismic profile into observation well 2 using a vibroseis sweep from 1-150 Hz. Figure 3 shows the source geometry for the 3D-VSP survey. Shots were centered on observation well 2 (green circle) and taken every 15 degrees along concentric circles with the radii increasing by 60 meters. An additional line of shots was taken along the trench at 53 degrees from east with a shot spacing of 10 meters.

The data were acquired using three component, 10 Hz, geophones along the trench with a receiver spacing of 10 meters and 324 levels of 1 Hz vectorseis 3C geophones in observation well 2, spaced at one meter intervals (figure 4). The modeled fibre loop is shown in figure 5(a) with the blue portions representing the straight fibre sections, and the red portions representing the helical fibre. Figure 5(b) shows a zoomed in portion of the geometry in figure 5(a) to provide a better representation of scale.

Taken together, this survey uses the source geometry in figure 3, the receiver geometry in figure 4, and the fibre loop in figure 5 and produces a four component (4C) dataset made up of particle velocity in the x,y, and z direction from the 3C geophones, and tangential strain from the DAS fibre. The transect of this dataset taken along the trench provides a good dataset for testing full waveform inversion using the complementary aspects of distributed acoustic sensors and three component geophones. This is because this transect contains both surface and downhole installations of both fibre and geophones. Future work will focus on developing FWI algorithms, using this data, to leverage the complementary aspects of DAS and 3C geophones.

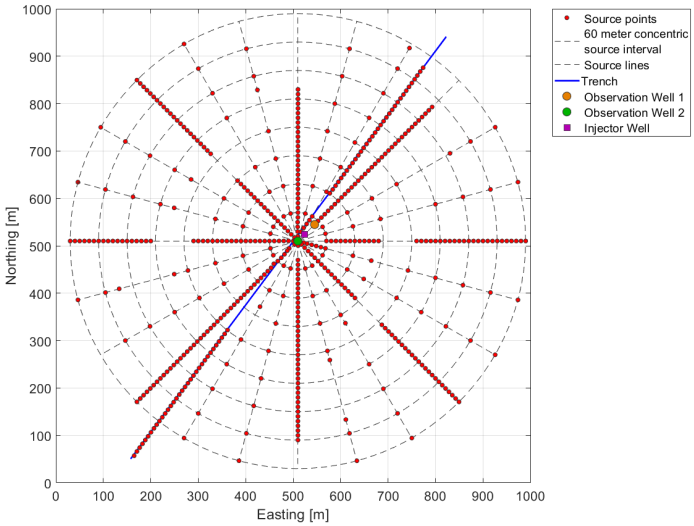

FIG. 3. Source geometry for 2018 walkaway-walkaround 3D VSP survey. Shot locations, shown by red circles were taken every 15 degrees along concentric circles with radii increasing by 60 meters. Shots centered on observation well 2 (green circle). Also shown are the postions of injector well (purple square), and observation well 1 (orange circle).

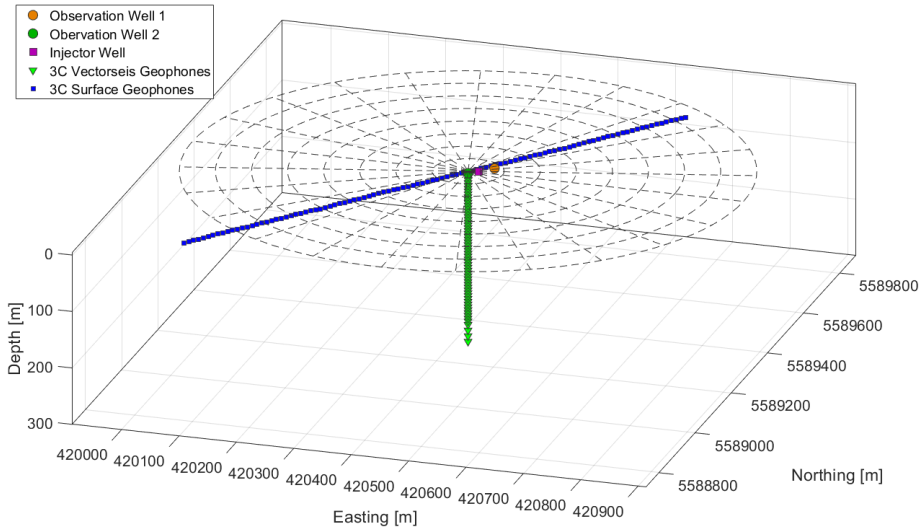

FIG. 4. Receiver geometry for 2018 walkaway-walkaround 3D VSP survey. Represented by blue squares are the 3C, 10 Hz surface geophones, colinear with the trench. The downhole 3C vectorseis geophones are shown by the green triangles.

MODELING THE 4C DATASET

The first step in any full waveform inversion work flow is the development of a forward model to generate synthetic data that may be compared against the observed data. Eaid et al. (2018) presented a method for modeling the strain response of distributed acoustic sensors based on a staggered grid, velocity-stress, finite difference method. This method relies on computations of the particle velocity and stress on a staggered grid to propagate the wavefield. Because strain rate, which is the quantity DAS measures, and the data geo-

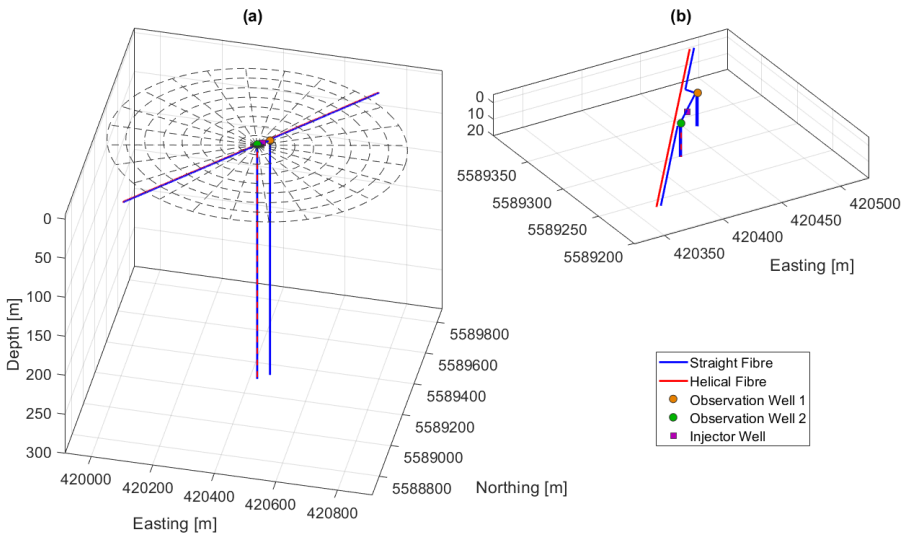

FIG. 5. (a) Modeled fibre geometry with source lines overlaid with black dotted lines. The portions of straight fibre are shown in blue, and the portions of helical fibre in red. (b) Zoom in of the fibre loop in (a) around the well used to highlight each portion of the fibre.

phones record both rely on measurements of particle velocity, this method is well suited to modeling the 4C data.

Velocity-stress finite difference method

The velocity-stress finite difference method utilizes a staggered grid and alternates between solving the elastodynamic equation of motion for particle velocity, equation (1), and the time derivative of Hooke's Law for stress, equation (2), to propagate the wavefield,

$$\rho \frac{\partial \dot{u}_i}{\partial t} = \nabla \cdot \sigma + f_i \tag{1}$$

$$\frac{\partial \sigma_{ij}}{\partial t} = C_{ijkl} \dot{\epsilon}_{kl}. \tag{2}$$

Where $\dot{u}$ is the particle velocity, σ the stress, and $\dot{\epsilon}$ the strain rate. The strain rate in equation (2) is computed by taking the time derivative of the strain tensor formula,

$$\dot{\epsilon}_{kl} = \frac{\partial \epsilon_{kl}}{\partial t} = \left(\frac{\partial \dot{u}_k}{\partial x_l} + \frac{\partial \dot{u}_l}{\partial x_k} \right). \tag{3}$$

Equation (1), supplies the particle velocity in the x, y, and z directions, and provides a method of directly computing all three components of the 3C geophone data. The strain rate field can be computed through spatial derivatives of the same particle velocities, as shown in equation (3). However, this is not the strain-rate that distributed acoustic sensors

record. Due to the rigidity of optical fibres, they are only sensitive to wavefields that induce tangential strain. Equation (3) provides strain rate in the given choice of field coordinates, in this case, inline, crossline, and depth. The DAS response is computed by rotating this field into a tangent, normal, and binormal coordinate system that varies along the fibre (Eaid et al., 2018),

$$\dot{\boldsymbol{\epsilon}}_{tnb} = \mathbf{R}\dot{\boldsymbol{\epsilon}}_{xyz}\mathbf{R}^{\mathrm{T}} \tag{4}$$

Equation (4) provides the strain rate tensor in a coordinate system which varies along the fibre axis. Due to the fibre rigidity, the only measured component of this strain rate that is nonzero is given by the element in the first row and first column of the strain rate tensor ($\dot{\boldsymbol{\epsilon}}_{tt}$). Taken together, equations (1) and (4) provide the four components that are required to investigate the complementary aspects of three component geophone and distributed acoustic sensing data

Modeled data from CaMI field site

In this issue, Hall et al. (2018), covers the walkaway-walkaround VSP, and specifically the processing steps in more detail. First breaks were picked from the nearest offset shot to observation well 2 on the vertical component of the vectorseis geophones. Using these first breaks, a preliminary p-wave velocity model was constructed as a basis for modeling the CaMI field data. A shear-wave velocity model was computed using the average vp-vs ratio from well logs in the area (v_p/v_s = 2.10). Densities were calculated using Gardner's relation with the parameters α and m derived from least-squares regression using the same well logs ($\alpha = 192$, $m = 0.32$). The 1D models in figure 6 were then used to a build a 3D isotropic model for elastic wave propagation.

Wavefields were propagated through the 3D model using equations (1) and (2) on a staggered grid to model the geophone and fibre data from the CaMI field research station. Figure 7 shows the location of shot number 13204 (red circle), the last shot on the northeast end of the trench, which was used for modeling. A 25Hz wavelet was chosen based on the vibroseis sweep.

To model a comparable dataset to the CaMI field data the v_x and v_y components of the particle velocity were rotated into radial and transverse components.

$$\begin{bmatrix} v_R \\ v_T \end{bmatrix} = \begin{bmatrix} \cos\theta & \sin\theta \\ -\sin\theta & \cos\theta \end{bmatrix} \begin{bmatrix} v_x \\ v_y \end{bmatrix} \tag{5}$$

Figure 8 shows the data modeled using the parameters in figure 6 and the shot in figure 7. The top row shows the 3 components of the geophone data, while the bottom row shows the fibre data over one length of the well. Figure 8 (a) shows the vertical component, (b) the radial, and (c) the transverse. Figure 8(d) shows the data from the straight fibre, while (e) shows the data from the helical fibre. Figure 9 presents the same components for the recording instruments along the trench.

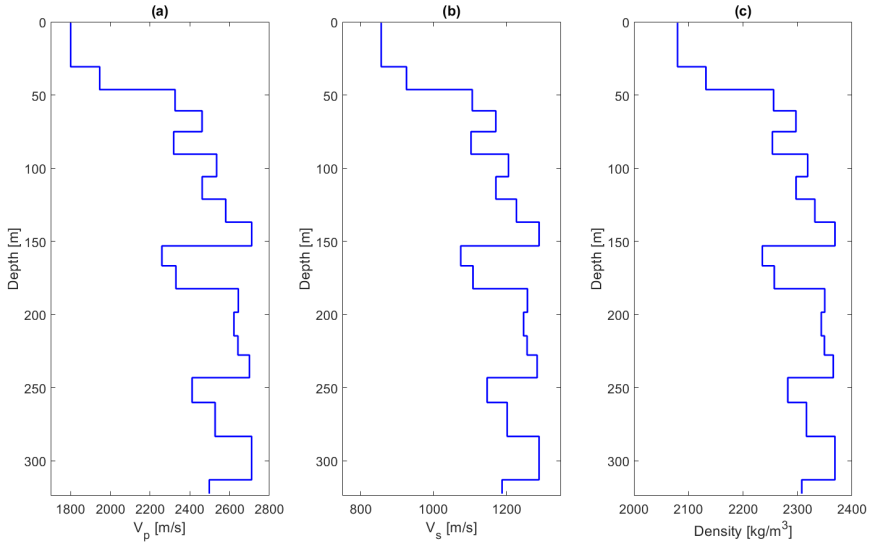

FIG. 6. (a) P-wave velocity model computed from first breaks picked on vertical component of the geophones in observation well 2 from a near-offset shot, (b) s-wave velocity model computed from (a) using a vp-vs ratio of 2.10, (c) density model computed using Gardner's relation with velocities given by (a) and using $\alpha = 192$, $m = 0.32$.

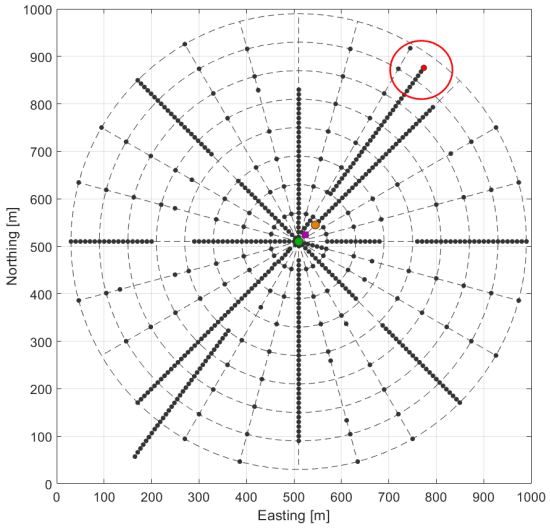

FIG. 7. Shot geometry for 2018 walkaway-walkaround VSP. The shot point to the northeast, shown in red was the one chosen for modelling of the fibre and geophone data.

These data were then altered to make data that was comparable to the field data, which allows us to highlight the complementary aspects of geophone and DAS data. Random noise was added to both the geophone and DAS data to highlight the reduced signal-to-noise ratio of the DAS data. The geophone data were then band pass filtered from 10-150 Hz using a Butterworth filter to simulate the effect of 10 Hz geophones. Distributed acoustic sensing data has been shown to contain useful frequencies down to 0.5 Hz (Jin and Roy, 2017). Therefore the DAS data were only low pass filtered at 150 Hz. Figures 10 and 11 show the results of applying this workflow to the data in figures 8 and 9 respectively.

Figure 12 shows a comparison between the modeled geophone data, and the field data recorded in September. The top row shows the vertical component, with the field data shown in (a) and the modeled data in (b), while the bottom row shows the radial component with the field data in (c) and the modeled data in (d).

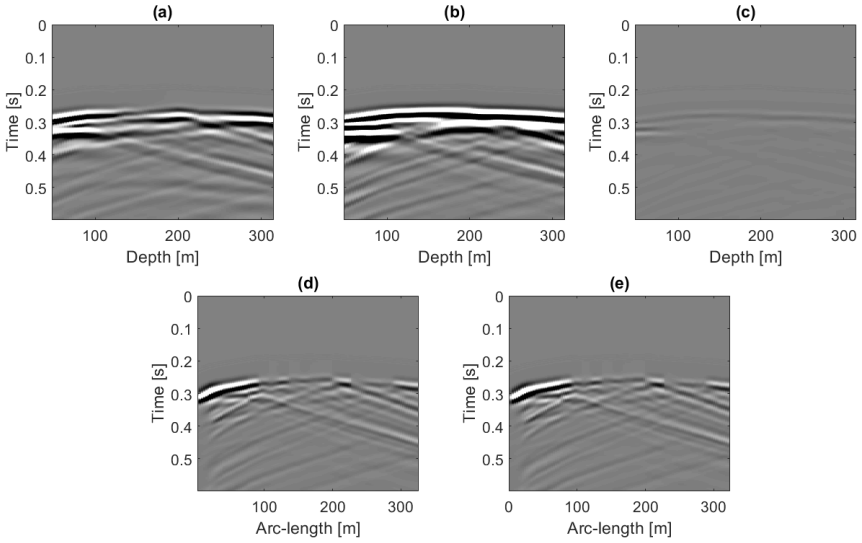

FIG. 8. Data from modelling using the shot point of figure 7 with a 25 Hz Ricker wavelet for recording instruments in observation well 2. The top row shows the data from the 3C geophones, and the bottom row shows the fibre data for one length of the well. (a) Vertical component, (b) radial component, (c) transverse component, (d) straight fibre data, (e) helical fibre data.

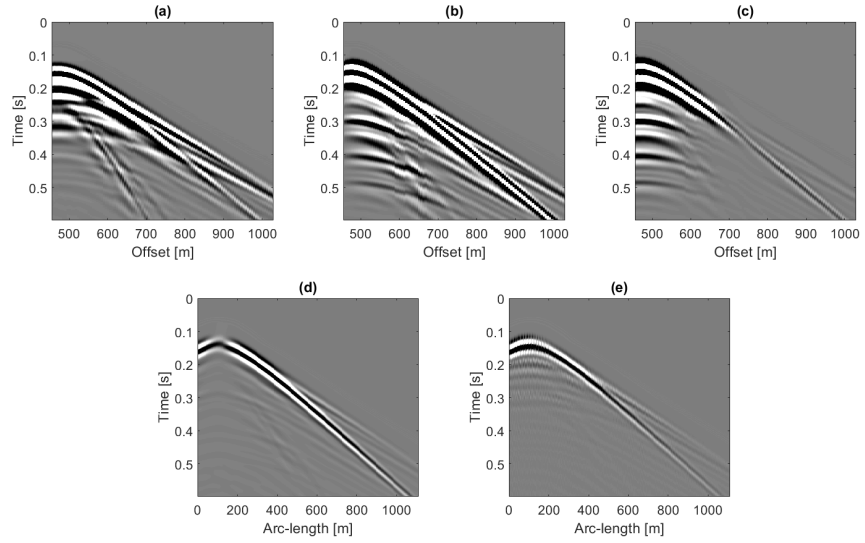

FIG. 9. Data from modelling using the shot point of figure 7 with a 25 Hz wavelet for recording instruments in the trench. The top row shows the data from the 3C geophones, and the bottom row shows the fibre data. (a) Vertical component, (b) radial component, (c) transverse component, (d) straight fibre data, (e) helical fibre data.

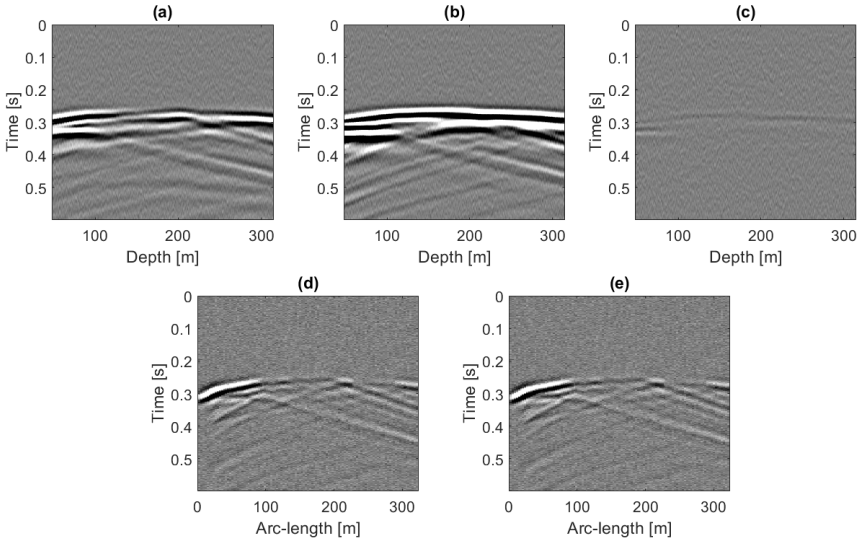

FIG. 10. Data from modelling with added noise and band pass filtering, using the shot point of figure 7 with a 25 Hz wavelet for recording instruments in observation well 2. The top row shows the data from the 3C geophones, and the bottom row shows the fibre data for one length of the well. (a) Vertical component, (b) radial component, (c) transverse component, (d) straight fibre data, (e) helical fibre data.

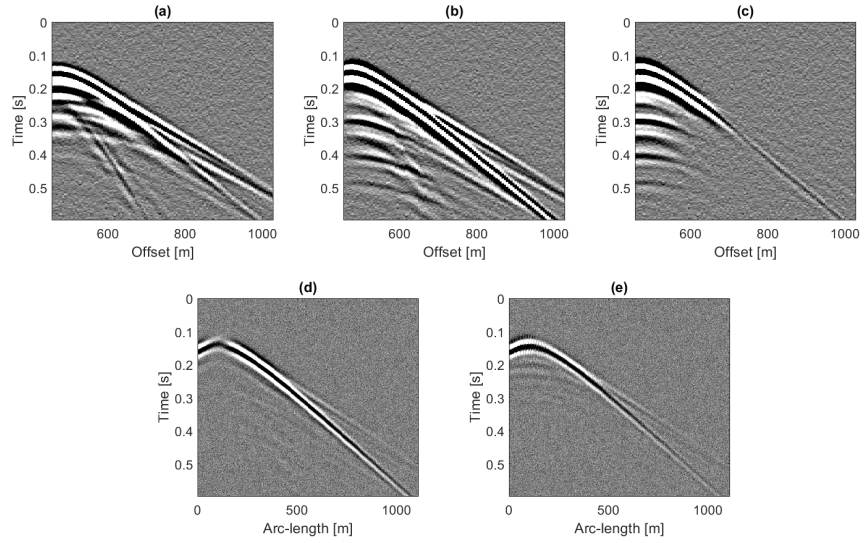

FIG. 11. Data from modelling with added noise and band pass filtering, using the shot point of figure 7 with a 25 Hz wavelet for recording instruments in the trench. The top row shows the data from the 3C geophones, and the bottom row shows the fibre data. (a) Vertical component, (b) radial component, (c) transverse component, (d) straight fibre data, (e) helical fibre data.

DISCUSSION

Figures 8 and 9 show the four components that we postulate as sharing complementary aspects that could lead to a more robust form of FWI. These four components were then subjected to a processing workflow in order to create a more realistic dataset, by adding random noise, and band pass filtering each component according to the bandwidth expected

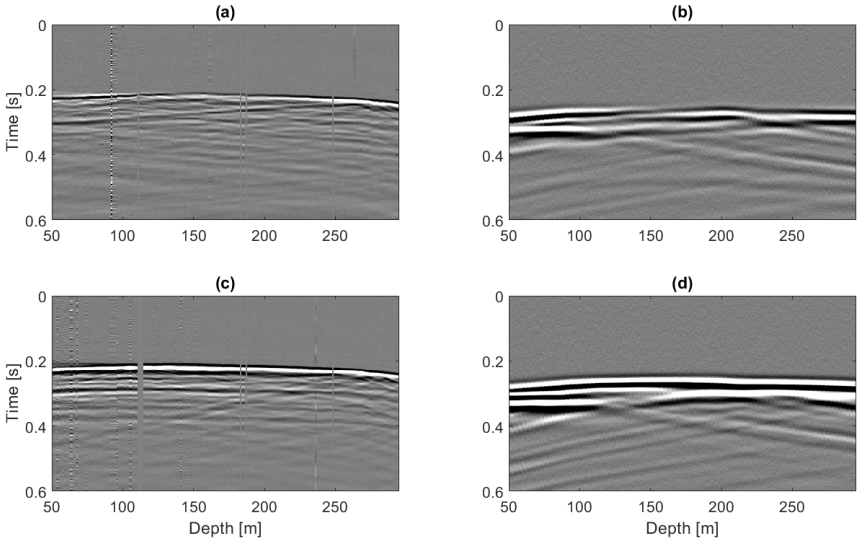

FIG. 12. Comparison of field, and modeled data from the 3C geophones in Observation well 2. (a) Vertical component of the field data, (b) modeled vertical component, (c) radial component of the field data, (d) modeled radial component.

from the data. The data resulting from this processing are shown in figure 10 and 11.

Figure 10 shows the processed data for the geophones and fibre in observation well 2. Because the fibre measures tangential strain, and the fibre is in a vertical well, the data from the straight fibre in figure 10(d) are comparable to the the vertical component of the geophone in figure 10. Comparing figure 10(a) and 10(d), similar events exist between the DAS and geophone data. Thus, the fibre is only supplying one component of the wavefield, along the tangent of the fibre. The helical fibre provides another dataset, but once again only supplies one tangential component. Both fibre datasets also have a worse signal to noise ratio than the geophone data. Despite these shortcomings, DAS supplies data with a denser spatial sampling, 0.25 meters instead of the one meter geophones, with an increased bandwidth. Figure 13 shows the average amplitude spectrum for the fibre data, bandpass filtered from 0-150 Hz in blue and the geophone data filtered from 10-150 Hz in red. While the spectra are similar, the improved bandwidth, particularly at low frequency of the DAS data is beneficial for full waveform inversion.

The three components supplied by the geophones provide a superior sampling of the elastic wave modes, with higher signal to noise ratio. However, the three components are supplied at a narrower bandwidth with a sparser sampling which can be of detriment to FWI. DAS supplies data with a better bandwidth that is more densely sampled. On its own, neither dataset is perfect from a full waveform inversion perspective. However, taken together both share complementary aspects that when coupled should improve the quality of the information recovered from FWI.

Figure 11 shows the processed data from the geophones on the trench and the fibre in the trench. The results of this are similar to the results from observation well 2. However, this case presents subtle differences that contain implications for FWI. In this case the straight fibre is more akin to the radial component since the fibre tangent, and radial com-

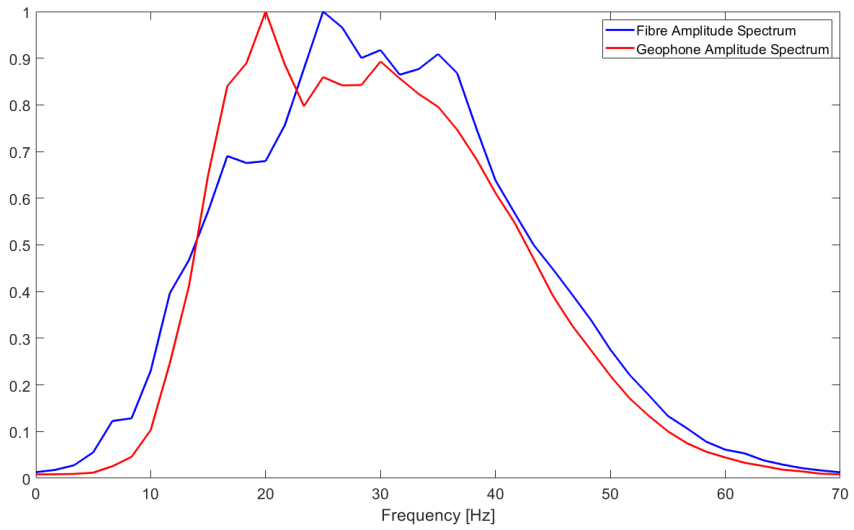

FIG. 13. Average amplitude spectra of bandpass filtered DAS data (blue) and geophone data (red).

ponent are parallel to the trench. Similar to the well, the geophones supply three elastic components at a high SNR, while the DAS provides a denser sampling at a wider bandwidth. What is important in this case is that DAS poorly images the reflected wave data because the reflections are incident at angles that are mostly normal to the fibre axis, and do not induce tangential strain. The helical fibre helps correct for this, but still cannot image the reflections with as high a fidelity as the geophone data. However, with an increased spatial sampling DAS better images the direct arrival. Additionally, Mills (2017) showed that dense spatial sampling is crucial for complete imaging of near surface waves, and accurate inversion for near surface velocity. In this case the two datasets are further complimentary from the perspective that each is more appropriate for imaging a certain wave type. Geophones provide a better image of the reflections, while DAS provides a more complete image of the surface waves. Both surface waves and reflections are crucial for robust FWI, and these two datasets taken together should improve our inversion result.

Figure 12 shows a comparison between the field data recorded using the 3C geophones in observation well 2 and the modeled geophone data for the vertical component in the top row and the radial component in the bottom row. The field data and modeled data share similarities which is encouraging. The first breaks of both vertical and radial component are comparable between the two datasets, indicating the model we used is a good representation of the subsurface as a starting block for inversion. Although the modeled data lacks the detail of the field data, some of the major reflections are represented in the modeled data, indicating some of the major reflectors have been modeled. The differences between the two are partly caused because the models were computed from first breaks at observation well 2, while the data comes from a shot with 450 meters offset to the well. Additionally, the first breaks do not provide a perfect representation of the velocity model. This fact motivates the need for full waveform inversion of the CaMI field research station model, which could provide a good baseline model for the CO_2 sequestration.

ACKNOWLEDGMENTS

The authors would like to thank the sponsors of the CREWES project as well NSERC under the grant CRDPJ 461179-13 for making this work possible through their financial support.

REFERENCES

Becker, M. W., Ciervo, C., and Coleman, T., 2018, Laboratory testing of low freqeuncy strain measured by distributed acoustic sensing: Society for Exploration Geophysicists 88th International Meeting.

Bunks, C., 1995, Multiscale seismic waveform inversion: Geophysics, **60**.

Eaid, M., Li, J., and Innanen, K., 2018, Modeling the response of shaped das fibres to microseismic moment tensor sources: Society for Exploration Geophysicists, Expanded Abstracts, 4698–4702.

Hall, K. W., Bertram, K. L., B., B. M., Innanen, K. A. H., and Lawton, D. C., 2018, Crewes 2018 multi-azimuth walk-away vsp field experiment: CREWES Research Reports, **30**, No. 16.

Jin, G., and Roy, B., 2017, Hydraulic-fracture geometry characterization using low-freqeuncy das signal: The Leading Edge, **36**.

Lailly, P., 1983, The seismic inverse problrm as a sequence of before stack migrations: Conference on Inverse Scattering, Theory and Application, Society for Industrial and Applied Mathematics, Expanded Abstracts.

Lawton, D. C., Bertram, M. B., Hall, K., Bertram, K., and Macquet, M., 2016, Near-surface velocity characterization at priddis and installation of fibre-optic cables at brooks, alberta: CREWES Research Reports, **28**, No. 42.

Mills, A., 2017, Application of near-surface seismic characterization to sparsely sampled data sets: Masters of Science Thesis.

Park, C. B., Miller, D. M., and Miura, H., 2002, Optimum field parameters of an masw survey: Society for Exploration Geophysicists, Expanded Abstracts.

Pratt, R., Shin, C., and Hicks, G., 1998, Guass-newton and full newton methods in frequency-space seismic waveform inversion: Geophysics Journal International.

Tarantola, A., 1984, Inversion of seismic reflection data in the acoustic approximation: Geophysics.

Virieux, J., and Operto, S., 2009, An overview of full-waveform inversion in exploration geophysics: Geophysics, **74**.